Surface Science 606 (2012) 1422–1425

Contents lists available at SciVerse ScienceDirect

Surface Science

journal homepage: www.elsevier.com/locate/susc

First-principles lattice dynamics, thermodynamics, and elasticity of Cr_2O_3

Yi Wang [a,*], Huazhi Fang [a], Chelsey L. Zacherl [a], Zhigang Mei [a], Shunli Shang [a], Long-Qing Chen [a], Paul D. Jablonski [b], Zi-Kui Liu [a]

[a] Materials Science and Engineering, The Pennsylvania State University, University Park, PA 16802, USA
[b] National Energy Technology Laboratory, Department of Energy, Albany, OR 97321, USA

ARTICLE INFO

Article history:
Received 20 September 2011
Accepted 7 May 2012
Available online 11 May 2012

Keywords:
Chromia
Phonon dispersions
Elasticity
Thermodynamics
Density functional calculations

ABSTRACT

We present the calculation of the lattice dynamics of chromia (Cr_2O_3), a typical Mott–Hubbard insulator, employing the first-principles density functional theory plus U approach. We first report the phonon dispersions at the theoretical equilibrium volume. Then the phonon density-of-states is calculated as a function of volume. Finally, the atomic volume, heat capacity, linear thermal expansion coefficient, bulk modulus, Grüneisen constant, and elastic constants are calculated as functions of temperature.

1. Introduction

Chromia (Cr_2O_3) [1] is a crystal from the corundum family that includes $A1_2O_3$, Fe_2O_3, Ti_2O_3, and V_2O_3, among others. Previous theoretical interests in these oxides are mainly focused on the transition from an insulator to a semiconductor or a metal [1]. Currently, research interests in Cr_2O_3 and $A1_2O_3$ are focused on their good corrosion resistant properties [2,3] as coatings of high temperature materials. To this end, the temperature dependences of thermodynamic and elastic properties are important for understanding the coating dynamics with respect to thermal stresses that arise from the mismatches between thermal expansion coefficients and elastic constants of the coating and substrate [4–8].

First-principles predictions of thermodynamic properties require the phonon density-of-states (DOS) as an input. Although the phonon dispersions of Cr_2O_3 have been measured experimentally and reported in the literature [1,9], corresponding first-principles calculation is lacking in part due to the difficulty to correctly handle Cr_2O_3 as a Mott–Hubbard insulator [10]. In this work, we report our first-principles study of lattice dynamics, thermodynamics, and elasticity of Cr_2O_3. The present work employs the mixed-space approach [11] to treat the splitting between longitudinal optical (LO) and transverse optical (TO) phonon modes and the density functional theory (DFT) + U method to account for the strong electron–electron correlations [12].

2. Theory

The present work adopts the direct method, or supercell approach, to obtain the phonon frequencies, i.e., the inter-atomic force constants are directly calculated in real-space using a supercell. Since Cr_2O_3 is a polar material, it is important to treat the contribution of the non-analytical term properly, which results in the LO–TO splitting. Recently, we developed a mixed-space approach to accurately determine the phonon frequencies [11,13] of a polar material using the supercell approach. To account for the contribution from the non-analytical term [14], the mixed-space approach treats the real-space force constant, $\Phi^{jk}_{\alpha\beta}$, between atom j in primitive cell M and atom k in primitive cell P as

$$\Phi^{jk}_{\alpha\beta}(M,P) = \phi^{jk}_{\alpha\beta}(M,P) + \frac{1}{N}\frac{4\pi e^2}{V}\frac{[\mathbf{q}\cdot\mathbf{Z}^*(j)]_\alpha[\mathbf{q}\cdot\mathbf{Z}^*(k)]_\beta}{\mathbf{q}\cdot\boldsymbol{\varepsilon}_\infty\cdot\mathbf{q}}| \quad (1)$$

where $\phi^{jk}_{\alpha\beta}$ is the contribution from short range interactions, N is the number of primitive unit cells in the supercell, V is the volume of the primitive unit cell, $\mathbf{q}$ is the wave vector, α and β are the Cartesian axes, $\mathbf{Z}^*(j)$ is the Born effective charge tensor of the jth atom in the primitive unit cell, and $\boldsymbol{\varepsilon}_\infty$ is the high frequency static dielectric tensor, i.e., the contribution to the dielectric permittivity tensor from the electronic polarization [15].

3. Computational details

The primitive unit cell of Cr_2O_3 is rhombohedral and contains 10 atoms [1]. As shown in Fig. 1a, the spins of the four Cr^+ ions in the unit cell of Cr_2O_3 are arranged along the [111] rhombohedral axis in

* Corresponding author.
E-mail address: yuw3@psu.edu (Y. Wang).

0039-6028/$ – see front matter
doi:10.1016/j.susc.2012.05.006

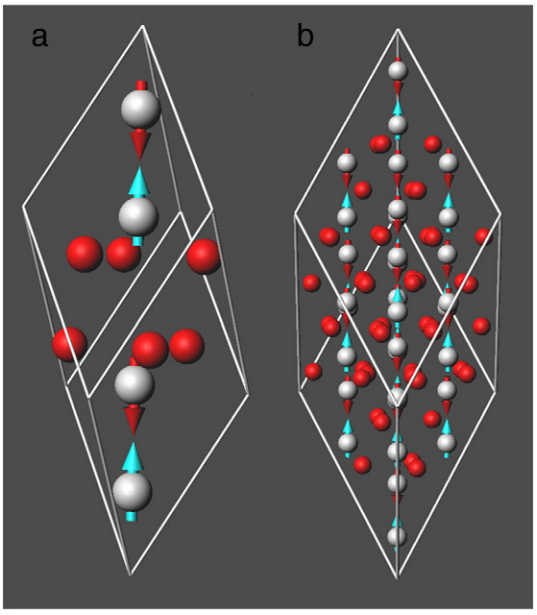

Fig. 1. (a) Primitive unit cell of Cr_2O_3; (b) used supercell of Cr_2O_3 for force constant calculation. Cr: balls with arrow; O: balls without arrow. The arrows mark the spin directions of the Cr atom.

a +−+− spin sequence [16–18]. When transformed into a hexagonal lattice, the Cr spins order antiferromagnetically both in the metal bilayers in the hexagonal basal plane, and in the normal plane [19,20] as shown Fig. 1b.

For first-principles static calculations at 0 K, we employ the projector-augmented wave (PAW) method [21,22] together with the rotationally invariant DFT + U method by Liechtenstein et al. [12] as implemented in the Vienna ab-initio simulation package (VASP, version 5.2). The calculated results using the DFT + U approach introduced by Liechtenstein et al. [12] depend on the effective on-site Coulomb (U) and exchange (J) parameters. We have chosen to use U = 4.5 eV and J = 1.0 for the *d* orbital of Cr. The calculated band gap is 3.36 eV which falls within the experimental range of 3.2–3.4 eV [23]. The local density approximation to the exchange-correlation functional as parameterized by Perdew and Zunger [24] is employed. For the calculation of the Born effective charge tensor, we use the procedure implemented in VASP 5.2 by Gajdos et al. [25] that determines the static ion-clamped dielectric matrix using density functional perturbation theory by following closely the original work of Baroni and Resta [26]. The 0 K static calculations are conducted at eight different volumes near the equilibrium. At each volume, both cell shape and internal atomic positions are optimized with a Γ-centered $11\times11\times11$ *k*-mesh, an energy cutoff of 500 eV, and a total energy convergence threshold of 10^{-8} eV. The present calculations show that the antiferromagnetic spin arrangement as shown in Fig. 1a with four Cr atoms in the primitive unit cell indeed leads to the lowest energy. For the calculation of real-space force constants, we use the linear-response approach together with an 80-atom $2\times2\times2$ supercell as shown in Fig. 1b, a Γ-centered $3\times3\times3$ *k*-mesh, and a reduced energy cutoff of 400 eV, which is accurate enough for the present purpose while saving computational resources. To get a smooth phonon DOS curve, sampling of the **q** space is made using a $100\times100\times100$ mesh, resulting in 30,000,000 phonon frequencies. In calculating the isothermal elastic constants, we have adopted the stress–strain approach [27,28] with a Γ-centered $15\times15\times15$ *k*-mesh and an energy cutoff of 500 eV. To mimic the temperature dependence of isothermal elastic constants, the "quasistatic" approximation [28] is adopted which assumes that the values of isothermal elastic constants depend only on volume.

4. Results and discussions

4.1. Geometric and dielectric properties

The calculated 0 K static side length and rhombohedral angle for Cr_2O_3 are 5.3412 Å and 55.10° respectively, which are within 0.2% of the experimental values of 5.35 Å and 55.15° [1]. The calculated high frequency static dielectric tensor and Born effective charge tensors for Cr_2O_3 are presented in Table 1. These data become the inputs to Eq. (1) for determining the contribution of the non-analytical term to the phonon frequencies. In particular, the calculated $\boldsymbol{\varepsilon}_\infty$ shows slight anisotropy, as evidenced by its *xx* and *yy* components being 6.000 and its *zz* component being 6.264. In comparison, the values from the spectroscopic estimates are 5.73 (perpendicular to the *c* or *z* direction) and 5.97 (parallel to *c* or *z* direction) by Lucovsky et al. [29] and are 6.1 and 6.2 by Onari et al. [30]. The anisotropy can be understood by the deviation of the rhombohedral angle from 60°, making the crystal anisotropic with respect to the hexagonal basal plane and the *c* direction. Furthermore, it is worth mentioning that by local point symmetry, all 6 oxygen atom sites are equivalent and all 4 chromium atom sites are equivalent. The differences in the values shown in the *xy*-plane among the data listed in Table 1 for the 6 oxygen atoms are due to the fact that the Cartesian axes are not the principal axes for a rhombohedral crystal. For the 4 chromium atoms, the differences in the values at the third decimal place are due to computational errors; typically on the order of 1% for DFT calculations.

4.2. Phonon spectra

In Fig. 2, we plot the calculated phonon dispersions of Cr_2O_3 together with experimental inelastic neutron scattering data [1,9]. For better visualization, the plot is made as the unfolded form of the Brillouin zone [1,9] along the major direction of Γ–A–Γ–Z–Γ–D. For a polar material, the longitudinal optical phonon frequencies depend on the direction that the Γ point is approached (see Cochran and Cowley [14]), as shown in Fig. 2 by the point connecting the A–Γ and Γ–Z dispersions.

Table 1
Calculated Born effective charge tensors for the Wyckoff positions of O(*x*,*y*,*z*) and Cr(*x*,*x*,*x*) and the high frequency static dielectric tensor ($\boldsymbol{\varepsilon}_\infty$) for Cr_2O_3.

	xx	*yy*	*zz*	*xy*	*xz*	*yx*	*yz*	*zx*	*zy*
$\boldsymbol{\varepsilon}_\infty$	6.000	6.000	6.264	0	0	0	0	0	0
O(0.555,0.250,0.945)	−2.185	−1.864	−2.136	0.277	−0.384	0.278	−0.665	−0.457	−0.792
O(0.945,0.555,0.250)	−1.704	−2.345	−2.136	0	0.767	0	0	0.915	0
O(0.250,0.945,0.555)	−2.185	−1.864	−2.136	−0.278	−0.383	−0.278	0.665	−0.458	0.792
O(0.445,0.750,0.055)	−2.185	−1.865	−2.136	0.278	−0.383	0.277	−0.664	−0.458	−0.792
O(0.055,0.445,0.750)	−1.704	−2.345	−2.136	0	0.767	0	0	0.915	0
O(0.750,0.055,0.445)	−2.185	−1.865	−2.136	−0.277	−0.384	−0.277	0.664	−0.457	0.792
Cr(0.152,0.152,0.152)	3.038	3.035	3.204	−0.243	0	0.244	0	0	0
Cr(0.348,0.348,0.348)	3.035	3.035	3.203	0.247	0	−0.244	0	0	0
Cr(0.848,0.848,0.848)	3.035	3.038	3.203	−0.247	0	0.246	0	0	0
Cr(0.652,0.652,0.652)	3.038	3.038	3.204	0.243	0	−0.246	0	0	0

In Fig. 3, the calculated total phonon DOS is plotted. A clear phonon energy gap is seen around 15 THz. Furthermore, it is known [31] that in most inelastic neutron experiments, the neutron cross section weighted phonon DOS is directly measured. For the purposes of prediction and comparison to future experiments, in Fig. 3 we also plot the calculated atom projected partial DOS and generalized phonon DOS [31], i.e., $\mathrm{GDOS} = \sum_i \frac{\sigma_i}{M_i} \mathrm{pDOS}_i$ where σ_i, M_i, and pDOS_i represent the atomic scattering cross section [32], the atomic mass, and the partial phonon DOS with $i = (\mathrm{Cr}, \mathrm{O})$, respectively. We see that the contribution from chromium dominates in the frequency region lower than the phonon energy gap while the contribution from oxygen dominates in the frequency region higher than the phonon energy gap. In the low frequency region, the GDOS is lower than the DOS, as evidenced by $\sigma_{Cr}/M_{Cr} = 0.067$ for chromium, which is substantially smaller than that of oxygen, which has a value of $\sigma_O/M_O = 0.265$.

4.3. Thermodynamic properties

With the phonon DOS calculated as a function of volume, the thermodynamic properties can be calculated in a straightforward manner following the standard procedure [33], which utilizes both the 0 K static energy and the phonon DOS to calculate thermodynamic data as a function of temperature. Fig. 4 illustrates the calculated heat capacity together with the available experimental data [10,34–36]. The peak positioned at 307 K among the measured data is due to the Néel transition that has not been accounted for in the present study. We note that, at present, there is no existing computationally affordable first-principles framework which can be employed to accurately calculate the magnetic contribution to the heat capacity. Therefore, it is not surprising that the calculated heat capacity is in poor agreement with the experimental results [35,36] in the vicinity of the Néel transition. However, very good agreement with the experimental data is observed from 0 K to about 100 K and also above 700 K.

Thermal expansion is another key thermodynamic property of Cr_2O_3 when it is applied as a high temperature coating material [7]. Fig. 5 compares the calculated linear thermal expansion coefficient of Cr_2O_3 with measured data by Huntz et al. [4]. The calculation of the thermal expansion coefficient is sensitive to the evaluation of the second order derivative of the free-energy. In one hand, the overall agreement with experiment is acceptable if compared with those for Ni–Al system in our previous work [33]. In the other hand, it is noted that the measured linear thermal expansion coefficients [4–6] of Cr_2O_3 are quite scattered in the range of 5.7×10^{-6}/K and 10.75×10^{-6}/K.

Other useful thermodynamic quantities for high temperature applications of Cr_2O_3 are the atomic volume, the bulk modulus, and

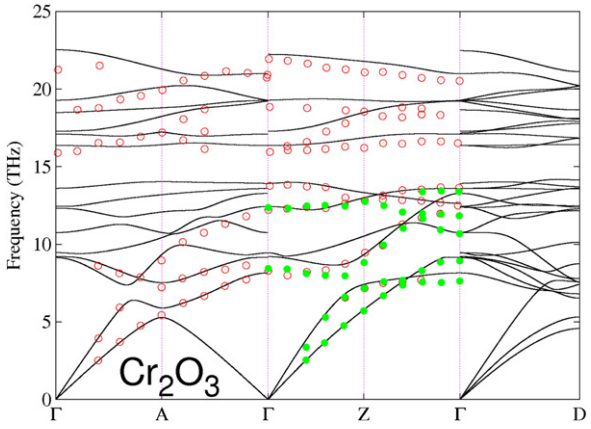

Fig. 2. Phonon dispersions of Cr_2O_3. The solid lines represent the present calculation, the open circles and solid circles represent, respectively, the reported inelastic neutron scattering data by May et al. [9] and Schober et al. [1].

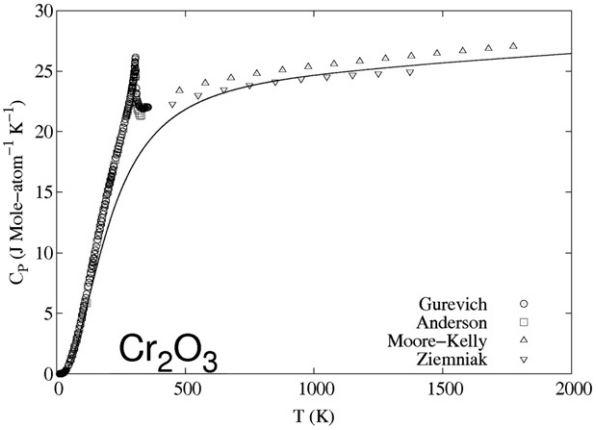

Fig. 4. Heat capacities of Cr_2O_3 with the solid line from the present calculation, and the circles, squares, up-triangles, and down-triangles representing the measured data by Gurevich et al. [10], Anderson [34], Moore and Kelly [35], and Ziemniak et al. [36] respectively.

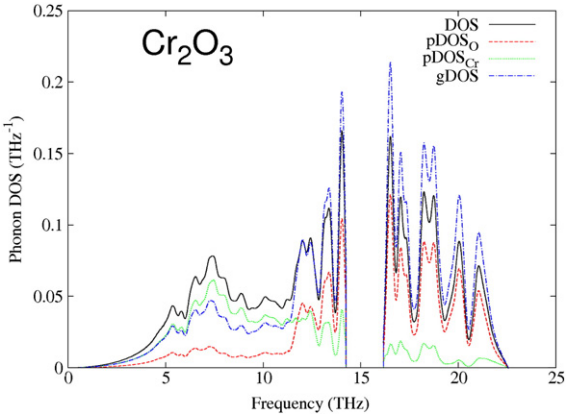

Fig. 3. Calculated phonon DOS (black solid line), partial DOS from oxygen (red dotted line), partial DOS from chromium (green dashed line), and the generalized phonon DOS (blue dotted–dash line) for Cr_2O_3.

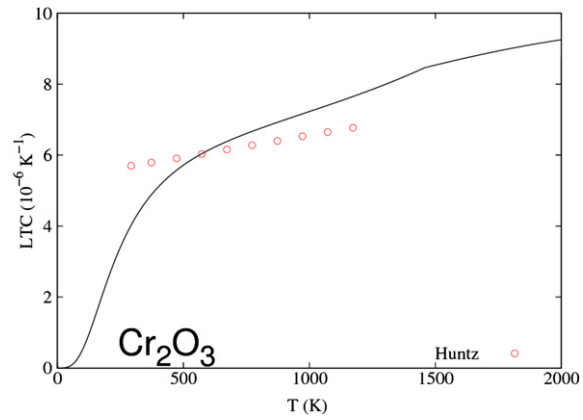

Fig. 5. Linear thermal expansion coefficient of Cr_2O_3 with the solid line from the present calculation and the open circles representing the measured data by Huntz et al. [4].

the thermodynamic Grüneisen constant. The calculated results for these parameters from 300 to 1400 K are collected in Table 2 together with the calculated heat capacity and linear thermal expansion coefficient. For comparison, our calculated bulk modulus of 238 GPa for Cr_2O_3 at 300 K compares well with the measured bulk moduli for Cr_2O_3 that are scattered in the range of 222–240 GPa [8,37].

4.4. Elasticity

Finally, the calculated isothermal elastic constants of Cr_2O_3 are compiled in Table 3. In particular, the calculated isothermal elastic constants, c_{ij}^Ts, are in excellent agreement with those from the ultrasonic measurement (isentropic) reported by Alberts and Boeyens [38]. Based on the calculated c_{ij}^Ts, an attempt is also made to calculate the Young's modulus and shear modulus of polycrystalline Cr_2O_3 according to Voigt's expressions [39], included in Table 3. The calculated Young's modulus of 316 GPa compares well with the experimental value of 314 GPa as cited by Pina et al. [40].

5. Conclusions

In summary, we have managed to reproduce physical properties of bulk chromia using DFT + U approach. We show the calculated phonon dispersions of this Mott–Hubbard insulator using the supercell approach with the recently developed mixed-space approach [11] for phonons of polar materials. Furthermore, based on the calculated phonon DOS and the 0 K static energy, we predict the thermodynamic properties of Cr_2O_3 including the atomic volume, bulk modulus, Grüneisen constant, heat capacity, and linear thermal expansion coefficient as a function of temperature. Last, the elastic constants of Cr_2O_3, as a function of temperature, are calculated using the quasistatic approximation [28]. The calculated elastic constants compare well with the available experimental data while the calculated heat capacity shows a deviation from the experimental data due to the fact that the present calculations have not considered the effects from the magnetic transition at 307 K.

Table 2
Calculated atomic volume V (Å^3/atom), linear thermal expansion coefficient α (10^{-6} K^{-1}), constant pressure heat capacity C_p (J/mole-atom K^{-1}), bulk modulus B_T (GPa), and Grüneisen constant γ for Cr_2O_3 as a function of temperature T (K).

T	V	α	C_p	B_T	γ
300	9.6441	4.12	17.33	238	0.988
400	9.6576	5.10	20.19	235	1.043
500	9.6733	5.72	21.83	232	1.073
600	9.6906	6.14	22.84	229	1.092
700	9.7089	6.47	23.52	226	1.106
800	9.7282	6.74	24.00	222	1.118
900	9.7482	6.99	24.36	219	1.128
1000	9.7691	7.23	24.66	215	1.138
1100	9.7906	7.47	24.90	210	1.148
1200	9.8129	7.72	25.12	206	1.158
1300	9.8361	7.99	25.32	201	1.169
1400	9.8601	8.28	25.50	196	1.180

Table 3
Calculated isothermal elastic constant c_{ij}^T (GPa), Young's modulus E (GPa), and shear modulus G (GPa) for Cr_2O_3 as a function of temperature T (K). The data in the parentheses are the measured isentropic elastic constants by Alberts and Boeyens [38] and Young's modulus as cited by Pina et al. [40] at room temperature.

T	c_{11}^T	c_{12}^T	c_{13}^T	c_{14}^T	c_{33}^T	c_{44}^T	E	G
300	373 (374)	160 (148)	178 (175)	−21 (−19)	349 (362)	160 (159)	316 (314)	124
400	371	159	176	−21	348	160	316	124
500	370	157	175	−21	347	159	315	124
600	368	155	173	−21	345	159	314	123
700	366	153	171	−21	343	158	314	123
800	364	151	168	−20	342	158	313	123
900	361	149	166	−20	340	157	312	123
1000	359	147	164	−20	338	156	311	123
1100	357	145	161	−20	336	156	310	122
1200	355	142	159	−19	334	155	309	122
1300	352	140	156	−19	332	154	308	122
1400	350	138	154	−19	330	154	307	122

Acknowledgments

This work was supported financially by the National Energy Technology Laboratory (grant no. 2010-SC-RES-30033026 and the RES contract DE-FE00400 in Turbines) in the United States, DOE Basic Sciences under grant no. DOE DE-FG02-07ER46417 (Yi Wang and Chen), and in part supported by instrumentation funded by the National Science Foundation through grant OCI-0821527. Calculations were also conducted at the National Energy Research Scientific Computing Center, which is supported by the Office of Science of the U.S. Department of Energy under contract no. DE-AC02-05CH11231.

References

[1] H. Schober, T. May, B. Dorner, D. Strauch, U. Steigenberger, Y. Morrii, Z. Phys. B 98 (1995) 197.
[2] J. Stringer, Mater. Sci. Eng., A 120 (1989) 129.
[3] E.A. Polman, T. Fransen, P.J. Gellings, J. Phys.-Condens. Matter 1 (1989) 4497.
[4] A.M. Huntz, S. Daghigh, A. Piant, J.L. Lebrun, Mater. Sci. Eng. A-Struct. Mater. Prop. Microstruct. Process. 248 (1998) 44.
[5] J. Mougin, A. Galerie, M. Dupeux, N. Rosman, G. Lucazeau, A.M. Huntz, L. Antoni, Mater. Corros. 53 (2002) 486.
[6] S. Osgerby, K. Berriche-Bouhanek, H.E. Evans, Mater. Sci. Eng. A-Struct. Mater. Prop. Microstruct. Process. 412 (2005) 182.
[7] X.L. Pang, K.W. Gao, H.S. Yang, L.J. Qiao, Y.B. Wang, A.A. Volinsky, Adv. Eng. Mater. 9 (2007) 594.
[8] L.R. Rossi, W.G. Lawrence, J. Am. Ceram. Soc. 53 (1970) 604.
[9] T. May, D. Strauch, H. Schober, B. Dorner, Physica B 234 (1997) 133.
[10] V.M. Gurevich, O.L. Kuskov, N.N. Smirnova, K.S. Gavrichev, A.V. Markin, Geochem. Int. 47 (2009) 1170.
[11] Y. Wang, J.J. Wang, W.Y. Wang, Z.G. Mei, S.L. Shang, L.Q. Chen, Z.K. Liu, J. Phys.-Condens. Matter 22 (2010) 202201.
[12] A.I. Liechtenstein, V.I. Anisimov, J. Zaanen, Phys. Rev. B 52 (1995) R5467.
[13] S.L. Shang, J.E. Saal, Z.G. Mei, Y. Wang, Z.K. Liu, J. Appl. Phys. 108 (2010) 123514.
[14] W. Cochran, R.A. Cowley, J. Phys. Chem. Solids 23 (1962) 447.
[15] S. Baroni, S. de Gironcoli, A. Dal Corso, P. Giannozzi, Rev. Mod. Phys. 73 (2001) 515.
[16] M. Catti, G. Sandrone, G. Valerio, R. Dovesi, J. Phys. Chem. Solids 57 (1996) 1735.
[17] D.E. Cox, G. Shirane, W.J. Takei, J. Phys. Chem. Solids 24 (1963) 405.
[18] T.G. Worlton, R.M. Brugger, R.B. Bennion, J. Phys. Chem. Solids 29 (1968) 435.
[19] J.E. Jaffe, M. Dupuis, M. Gutowski, Phys. Rev. B 69 (2004) 205106.
[20] N.J. Mosey, E.A. Carter, Acta Mater. 57 (2009) 2933.
[21] P.E. Blöchl, Phys. Rev. B 50 (1994) 17953.
[22] G. Kresse, D. Joubert, Phys. Rev. B 59 (1999) 1758.
[23] R. Zimmermann, P. Steiner, R. Claessen, F. Reinert, S. Hufner, P. Blaha, P. Dufek, J. Phys.-Condens. Matter 11 (1999) 1657.
[24] J.P. Perdew, A. Zunger, Phys. Rev. B 23 (1981) 5048.
[25] M. Gajdos, K. Hummer, G. Kresse, J. Furthmuller, F. Bechstedt, Phys. Rev. B 73 (2006) 045112.
[26] S. Baroni, R. Resta, Phys. Rev. B 33 (1986) 7017.
[27] S.L. Shang, Y. Wang, Z.K. Liu, Appl. Phys. Lett. 90 (2007) 052301.
[28] Y. Wang, J.J. Wang, H. Zhang, V.R. Manga, S.L. Shang, L.Q. Chen, Z.K. Liu, J. Phys.-Condens. Matter 22 (2010) 225404.
[29] G. Lucovsky, R.J. Sladek, J.W. Allen, Phys. Rev. B 16 (1977) 5452.
[30] S. Onari, T. Arai, K. Kudo, Phys. Rev. B 16 (1977) 1717.
[31] M. Zbiri, H. Schober, M.R. Johnson, S. Rols, R. Mittal, Y.X. Su, M. Rotter, D. Johrendt, Phys. Rev. B 79 (2009) 064511.
[32] V.F. Sears, Neutron News 3 (1992) 26.
[33] Y. Wang, Z.K. Liu, L.Q. Chen, Acta Mater. 52 (2004) 2665.
[34] C.T. Anderson, J. Am. Chem. Soc. 59 (1937) 488.
[35] G.E. Moore, K.K. Kelly, U.S. Bureau of Mines Technical Report 662 (1944).
[36] S.E. Ziemniak, L.M. Anovitz, R.A. Castelli, W.D. Porter, J. Chem. Thermodyn. 39 (2007) 1474.
[37] S. Rekhi, L.S. Dubrovinsky, R. Ahuja, S.K. Saxena, B. Johansson, J. Alloys Compd. 302 (2000) 16.
[38] H.L. Alberts, J.C.A. Boeyens, J. Magn. Magn. Mater. 2 (1976) 327.
[39] P. Ravindran, L. Fast, P.A. Korzhavyi, B. Johansson, J. Wills, O. Eriksson, J. Appl. Phys. 84 (1998) 4891.
[40] J. Pina, A. Dias, J.L. Lebrun, Mater. Sci. Eng. A-Struct. Mater. Prop. Microstruct. Process. 267 (1999) 130.